ORIGINAL PAPER

Identification of rare earth elements in synthetic and natural monazite and xenotime by visible-to-shortwave infrared reflectance spectroscopy

A. H. Dijkstra[1] · W. H. Bakker[1] · F. Deon[2] · C. Marcatelli[3] · M. P. Plokker[4] · H. T. Hintzen[5]

Abstract

To support the role of proximal and remote sensing in geological rare earth element (REE) resource exploration, we studied the reflectance spectroscopy of synthetic single- and mixed-REE phosphate phases. Synthesis yielded monazite for the elements La to Gd, and xenotime for Dy to Lu and Y. Visible-to-shortwave infrared (350–2500 nm) reflectance spectra of synthetic single-REE monazites and xenotimes can be used to identify the ions responsible for the absorption features in natural monazites and xenotimes. Nd^{3+}, Pr^{3+} and Sm^{3+} produce the main absorption features in monazites. In natural xenotime, Dy^{3+}, Er^{3+}, Ho^{3+} and Tb^{3+} ions cause the prevalent absorptions. The majority of the REE-related absorption features are due to photons exciting electrons within the 4f subshell of the trivalent lanthanide ions to elevated energy levels resulting from spin-orbit coupling. There are small (< 20 nm) shifts in the wavelengths of these absorptions depending on the nature of the ligands. The energy levels are further split by crystal field effects, manifested in the reflectance spectra as closely spaced (~ 5–20 nm) multiplets within the larger absorption features. Superimposed on the electronic absorptions are vibrational absorptions in the H_2O molecule or within $[OH]^-$, $[CO_3]^{2-}$ and $[PO_4]^{3-}$ functional groups, but so far only the carbonate-related spectral features seem usable as a diagnostic tool in REE-bearing minerals. Altogether, our study creates a strengthened knowledge base for detection of REE using reflectance spectroscopy and provides a starting point for the identification of REE and their host minerals in mineral resources by means of hyperspectral methods.

Keywords Rare earth elements · Monazite · Xenotime · Spectroscopy · Mineralogy · Critical raw materials

✉ A. H. Dijkstra
  a.h.dijkstra@utwente.nl

1 Department of Applied Earth Sciences, Faculty of Geo-information Science & Earth Observation (ITC), University Twente, Enschede, The Netherlands

2 Section Geoenergy, Helmholtz Centre Potsdam, GeoForschungZentrum Postdam, Germany

3 Geoscience Laboratory, Faculty of Geo-information Science & Earth Observation (ITC), University Twente, Enschede, The Netherlands

4 Dutch Research Council (NWO), Winthontlaan 2, Utrecht, The Netherlands

5 Department of Radiation Science and Technology, Delft University of Technology, Delft, The Netherlands

Introduction

Rare earth element resources

The rare earth elements (REE), i.e., the lanthanides and yttrium, are critical raw materials for our modern society. The element scandium is also sometimes included in this group, but is not further considered below. The demand for REE is predicted to grow strongly as a result of the energy and mobility transitions, as the REE are essential for low-carbon energy and mobility solutions such as permanent magnets in electric generators and motors (Hund et al. 2020; European Commission Joint Research Centre 2020; International Energy Agency 2021). Concerns about the security of supply of REE, mainly due to the strong geographic concentration of mining and processing activities (Patrahau et al. 2020), have led to an increase in exploration activities worldwide in an attempt to diversify the source (e.g.,

Goodenough et al. 2016). While REE exploration and production since the 1960's has been focussed on rocks containing REE-carbonate minerals such as bastnäsite, there is again an increasing interest in REE-phosphates such as monazite and xenotime in both igneous, hydrothermal, and sedimentary rocks (and placers) as REE resources (Santana et al., 2015; Goodenough et al. 2016; Chen et al. 2017; Marien et al. 2018; Anenburg et al. 2018; Nazari-Dehkordi et al. 2020).

Recent studies have shown that reflectance spectroscopy, including imaging spectroscopy, is a promising tool to support detection and identification of REE-bearing minerals in exploration and mining, either in hyperspectral airborne- or UAV-based remote sensing (Rowan et al. 1986; Neave et al. 2016; Booysen et al. 2020; Jackisch et al., 2020), or in proximal sensing like scanning of outcrop or drill core samples (Turner et al. 2014a; Boesche et al. 2015, 2016; Coint and Dahlgren 2019; Qasim and Khan 2022). Very recently, next-generation hyperspectral satellites such as Prisma, EnMap and Gaofen-5 have come on-line which theoretically have the spectral resolution to detect the distinct absorption features of REE-bearing minerals. It has been well established that excitation of electrons in the 4f orbitals of the lanthanides produce deep and narrow absorptions at discrete wavelength of visible light, as well as in the near- and short-wave infrared, which makes reflectance spectroscopy particularly well suited to detect REE-bearing minerals (e.g., Turner et al. 2014b, 2016, 2018). So far, applications have relied almost exclusively on the clearly identifiable absorption features associated with the neodymium ion (Nd^{3+}) in minerals near 750 and 800 nm (e.g., Boesche et al. 2015, 2016; Coint and Dahlgren 2019; Qasim and Khan 2022; Fig. 1). We argue that spectral information resulting from several other lanthanides is underused, partly due to a lack of empirical reflectance spectroscopy data that can be used to link observed electronic absorption features in natural minerals to specific lanthanides.

Thus far, attributions of absorption features at specific wavelengths to discrete lanthanide elements are mainly based on reflectance spectra acquired on lanthanide oxide powders, not on carbonates or phosphates that resemble natural host minerals for the REE. Most absorption features in REE-minerals are controlled by intra-configurational 4f-4f transitions of electrons between energy levels determined by electron spin-orbit coupling in the trivalent lanthanide ions. The lanthanide 4f electrons are relatively shielded from the influence of surrounding ligands (e.g., O^{2-}) in minerals by the 5s, and 5p subshells; therefore, the crystal field

Fig. 1 Selected reflectance spectra for natural monazite crystals from USGS and GSC spectral libaries (Kokaly et al. 2017; Percival et al. 2019). Spectra are off-set for clarity and are re-scaled such that the absorption minima at near 800 nm have the same depth. Monazite: (1) Ione, California, US (GDS947); (2) Our collection, unknown location; (3) Petaca District, New Mexico, US (GDS957); (4) Siglo Veinte, Potosi, Bolivia (2178_NMC063108); (5) Betsiboka Valley, Madagascar (2179a_NMC063733a); (6) Elk Mountain, New Mexico, US (WS385); (7) Iveland, Setesdal, Norway (GDS955); (8) Gjerstad, Norway (2174_NMC018965). Xenotime: (9) Ivedestrand, Norway (2187_NMC018948); (10) Iveland, Setesdal, Norway (GDS966); (11) Novo Horizonte, Bahia, Brazil (2190_NMC067514)
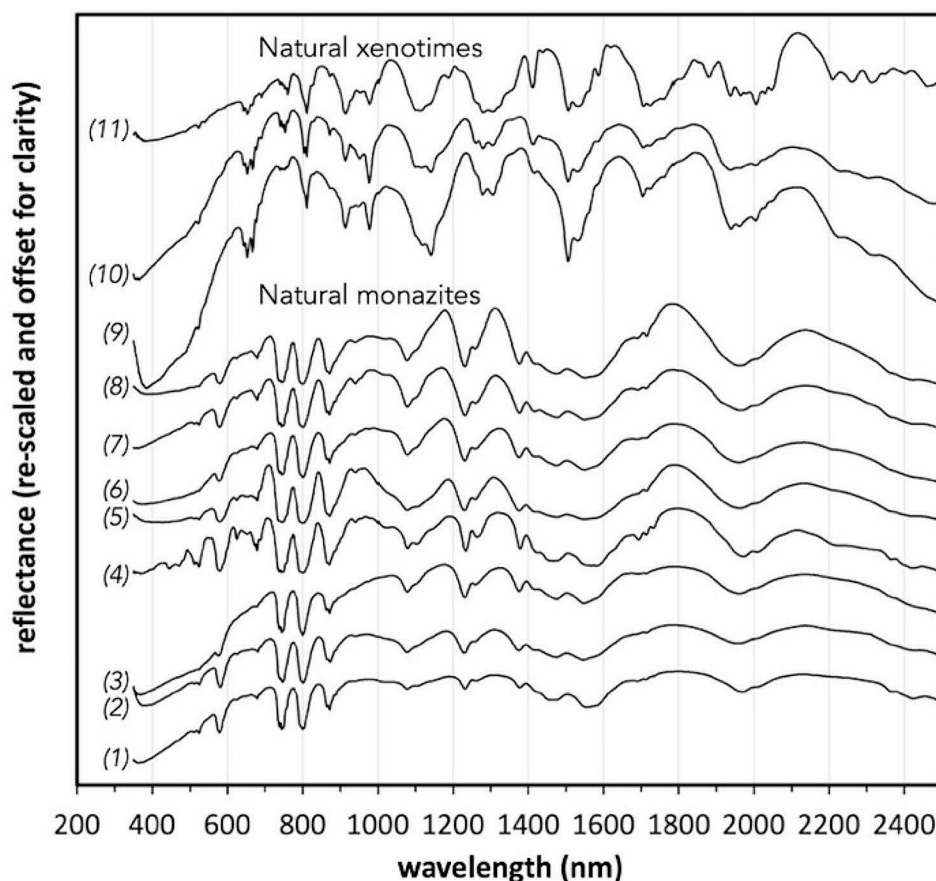
surrounding the lanthanide ion and the nature of the ligands have relatively little influence on the energy levels of the 4f electrons. In this notion, the reflectance spectrum of a lanthanide-bearing mineral would be insensitive to whether this mineral is a carbonate (e.g., bastnäsite), phosphate (e.g., monazite, xenotime), or silicate (e.g., eudialyte, britholite) (Clark 1999). However, the question to what extent this assumption is accurate for geologically important REE-minerals has gained little attention so far.

In this paper we present new 350–2500 nm wavelength reflectance spectroscopy data collected on laboratory-synthesized monazite and xenotime with controlled chemical compositions. Note that we use the mineral names monazite and xenotime in the strict geological-mineralogical sense, as phosphates with a monazite or xenotime crystal structure and the formula unit [REE]PO_4, where [REE] stand for one or more of the trivalent ions of the following elements: La, Ce, Pr, Nd, Sm, Eu, Gd, Tb, Dy, Ho, Er, Tm, Yb, Lu, as well as the non-lanthanide Y. This usage is in contrast to the materials sciences, where any compound with a monazite structure but different chemical formula unit (e.g., $CaSO_4$, $CeVO_4$, $LaAsO_4$, e.g., Clavier et al. 2011) is also referred to as 'monazite' as a shorthand for 'with monazite structure'. For simplicity we will refer to our synthetic compounds as 'minerals' because they are crystallographically identical and chemically similar (albeit with a more limited range of REE, and including single-REE phases) to naturally-occurring minerals, even if they are not 'formed in nature'. The crystal structures of the synthesized compounds are verified by X-ray powder diffraction and structural refinement. We also compare the reflectance spectra of few different Nd-bearing phases to assess the effect of the crystal field. Most importantly, we compare our synthetic phases to their natural counterpart minerals, which are always solid solutions of all the REE, and we define the most diagnostic spectral features that can find application in proximal and remote sensing of monazite- or xenotime-bearing rocks.

Reflectance spectra of natural monazite and xenotime

The mineral monazite is a monoclinic (space group P 2_1/n) anhydrous phosphate of REE in which the light REE (LREE, La to Gd) dominate, and in which the REE ions are 9-fold coordinated. The mineral xenotime is an anhydrous phosphate in which the heavy REE (HREE, Dy to Lu and Y) dominate; the smaller-radius HREE ions are 8-fold coordinated, leading to the higher tetragonal symmetry (space group I 4_1/amd). The most common hydrated REE phosphates, with general formula [REE]$PO_4 \cdot nH_2O$], are LREE-dominated rhabdophane (coordination 8 or 9) and HREE-dominated churchite (coordination 8), both

crystallizing in the monoclinic system (Mesbah et al. 2014; Clavier et al. 2018).

The reflectance spectra of natural monazite and xenotime, which contain all 14 natural lanthanides plus Y in variable abundances, are well known. Figure 1 shows selected reflectance spectra of natural monazites and xenotimes in the 350–2500 nm wavelength range (Kokaly et al. 2017; Percival et al. 2019). In this figure the spectra are re-scaled in such a way that the prominent absorption feature near 800 nm visible in both mineral types has approximately the same depth in all the spectra. The spectra show many additional absorption features with varying depths, which could suggest that they are not caused by the same element as the 800 nm features. Some prominent features seen in xenotime but not in monazite, e.g., those between 900 and 1000 nm, as well as the complex absorption near 670 nm, are probably caused by HREE. Likewise, the feature near 580 nm in monazite is probably due to LREE, as it is not obvious in xenotime. The absorption features at 750 and 800 nm, widely believed to be both caused by Nd^{3+} in monazite, have similar depths in monazite, but not in xenotime; this suggests a role for a different ion in xenotime. Moreover, the steepness of the drop in reflectance seen in all spectra at wavelengths < 600 nm is variable, especially within the xenotime group.

To gain a better understanding of these complex reflectance spectra, reflectance spectra of single-REE monazites are required; single-REE occupancy can only be achieved in lab-synthesized monazite and xenotime of the kind prepared in our project.

Electronic processes in lanthanide ions and reflectance spectroscopy

There is a wealth of literature describing lanthanide absorption and emission features in the visible, near- and shortwave infrared part of the electromagnetic spectrum in engineered materials, such as glasses, laser crystals, waveguides, and luminescent materials for lighting and display applications (e.g., Carnall et al. 1978; Liu & Jacquier, 2006; Eliseeva and Bünzli 2010; Semwal & Bhat, 2013; Reid 2016; Freidzon et al. 2018). However, with some notable exceptions (Turner et al. 2014a, b, 2016, 2018), there is only limited translation of these modern insights into the spectral geology and mineralogy literature. For instance, in the classical review papers of Hunt (1977) and Clark et al. (1990), often used as introductory texts into the field, the four electronic processes that are described are related to: crystal field effects, charge transfer, conduction band transfers and colour centres. While these processes probably play a role in lanthanide-bearing minerals, their contributions to reflectance spectra in the visible, near- and shortwave infrared are

only of secondary importance compared to that of another electronic process: the intraconfigurational excitation of electrons to energy levels within the same 4f subshell. This intraconfigurational excitation mechanism as the main cause for the sharp absorptions in lanthanide compounds was already known for decennia (e.g., Van Vleck 1937; Dieke et al. 1968). These different 4f energy levels result from the coupling between the angular magnetic momenta, i.e., the spin and the orbital motions, of electrons (e.g., Dieke et al. 1968; Carnall et al. 1978; Eliseeva and Bünzli 2010). It seems therefore appropriate to briefly review the key electronic processes here, and to set the record straight when it comes to the reflectance spectroscopy of monazite and xenotime.

In interpreting the main absorption features in monazite and xenotime caused by lanthanides, we follow the Russell-Saunders notion of the coupling of angular momenta of electrons leading to the different energy levels of the 4f orbitals (e.g., House 2020). The electron configurations of the typical trivalent lanthanide ion, Ln^{3+}, is {Xe} $4f^n$, with n ranging from zero for La to 14 for Lu. The element Y, which is an REE but not a lanthanide, does not have 4f orbitals, and in its trivalent state has fully-filled 3d, 4s, 4p orbitals.

Possible electronic energy states resulting from spin-orbit coupling can be referred to by their Russell-Saunders 'term symbol':

$$^{2S+1}L_J$$

Here, S is the total spin angular momentum, and $2S+1$ is referred to as the total spin multiplicity. L is the total orbital angular momentum ($L=0, 1, 2, 3, 4, 5, 6$ in f-shells). In the term symbol notation these L values are replaced by the capital letters S, P, D, F, G, H and I respectively. J is the total coupled spin and orbital angular momentum, which can range from $L+S$ down to $|L-S|$. Furthermore, Hund's rules are used to determine which of the possible states has the lowest energy (House 2020).

We show the example of the Nd^{3+} ion (Fig. 2), which has the {Xe} $4f^3 5d^0 6s^0$ electron configuration. The state with the highest spin multiplicity has the lowest energy, which is the case if all three 4f electrons have spin up (or all spin down) configuration, so $S_{max}=3·½$ and the total spin multiplicity $(2S+1)_{max}=4$, referred to as 'quartet'. The other option in this case is $S=½$ (two 4f electrons in spin up configuration, and one spin down, or vice versa), where the spin multiplicity is $2S+1=2$ ('doublet'), but this state has a higher energy than the quartet. For the same spin multiplicity, the term with the highest orbital angular momentum L has the lowest energy. Figure 2 shows that $L_{max}=6$, corresponding to the letter 'I'. The resulting ^4I term symbol is split into four 'LSJ levels', i.e., $J=L+S=15/2$,

$L+S$-1 = 13/2, $L+S$-2 = 11/2, and $|L-S|$=9/2. The 4f shell can contain a maximum of 14 electrons. Hund's rules state that if the 4f shell is less than half-filled, the lowest J has the lowest energy. So, for Nd^{3+} with three 4f electrons the ground state is $^4I_{9/2}$. The first energy levels above the ground state (in order of increasing energy) are all ^4I levels, labelled $^4I_{11/2}$, $^4I_{13/2}$ and $^4I_{15/2}$; above that we find the ^4F levels ($L=3$) $^4F_{3/2}$, $^4F_{5/2}$, $^4F_{7/2}$ and $^4F_{9/2}$, followed by – or partially overlapping with – various doublet levels (^2H, ^2G, ^2F, ^2D) at higher energies.

The splitting of the energy levels due to the SL terms is in the order of 1 eV; the spin-orbit coupled interactions split these levels further into LSJ levels separated from each other by energies in the order of 0.1 eV (Reid 2016). These levels are due to free-ion interactions and they are largely independent of the crystal field, i.e., independent of the nature of the ligands and the coordination. In a crystal field, the interactions of electrons with ligands lead to further splitting of the LSJ levels, with splitting energies in the order of 0.01 eV (Carnall et al. 1978; Reid 2016). This means that in the near-infrared part of a reflectance spectrum, LSJ levels are expressed as absorption features c. 50 nm apart, further split up as a result of crystal field splitting into smaller absorption features c. 5 nm apart; the latter subject to the nature of the crystal field.

In addition to these 4f-4f intra-configurational electronic transitions, we can also consider transitions between the $4f^n$ and $4f^{n-1}5d^1$ configurations, i.e., the excitation of a 4f electron to a 5d orbital. These transitions have high energies and only those of trivalent Ce^{3+}, Pr^{3+} and Tb^{3+} are commonly observed optically, typically in the ultraviolet domain (Eliseeva and Bünzli 2010). As the 5d orbitals extend much further out from the nucleus, they interact directly with ligands. Therefore, 5d crystal field splitting energies are much larger (40 times, Reid 2016) as compared to those of the 4f levels. Finally, charge-transfer transitions in the trivalent lanthanides are possible but it in general they have high energies and are typically observed in the ultraviolet part of the spectrum (Eliseeva and Bünzli 2010). However, below we provide evidence suggesting that a Ce^{4+}-related charge transfer process is in part responsible for the brown colour of natural monazite.

Methods and materials

Synthesis of rare earth element phosphate powders

REE-phosphates were synthesized by a precipitation of a hydrous phosphate followed by high-temperature transformation to the desired anhydrous phase. Therefore, starting REE oxides used were purchased from Strategic Elements,

Fig. 2 (**a**) Two worked-out examples of Russell-Saunders notation of energy levels of the 4f electrons in the Nd^{3+} ion with configuration {Xe} 4f3. See also text for discussion. Both examples are cases with three electrons spinning up, as shown by the three upward pointing arrows (so S = 3/2), but with different orbital angular momenta (L = 6 and L = 3), and different spin-orbit coupling levels J. The $^4I_{9/2}$ level is the one with the lowest energy, i.e., the ground state for the Nd^{3+} ion. (**b**) Schematic representation of the energy splitting effects due to coulomb-type electron-electron interactions (^{2S+1}L terms, i.e., ^4I, ^4F, ^2H, ^4G, ...), further splitting into $^{2S+1}L_J$ levels due to spin-orbit coupling (^2H and ^2K levels omitted for clarity, but see Fig. 9 for their positions), and further splitting into so-called Stark levels due to crystal field effects. Relative positions of $^{2S+1}L_J$ levels are based on data from Carnall et al. (1978); number of crystal field levels per $^{2S+1}L_J$ level are for non-cubic site symmetry (Eliseeva and Bünzli 2010). Energy levels are not to scale, but order-of-magnitude values of splitting energies (in eV) are indicated. Two electronic transitions, from the ground state $^4I_{9/2}$ to $^4F_{7/2}$ and $^4F_{5/2}$ are highlighted on the right; these can be achieved by absorption of photons with wavelengths of ~750 and ~800 nm respectively
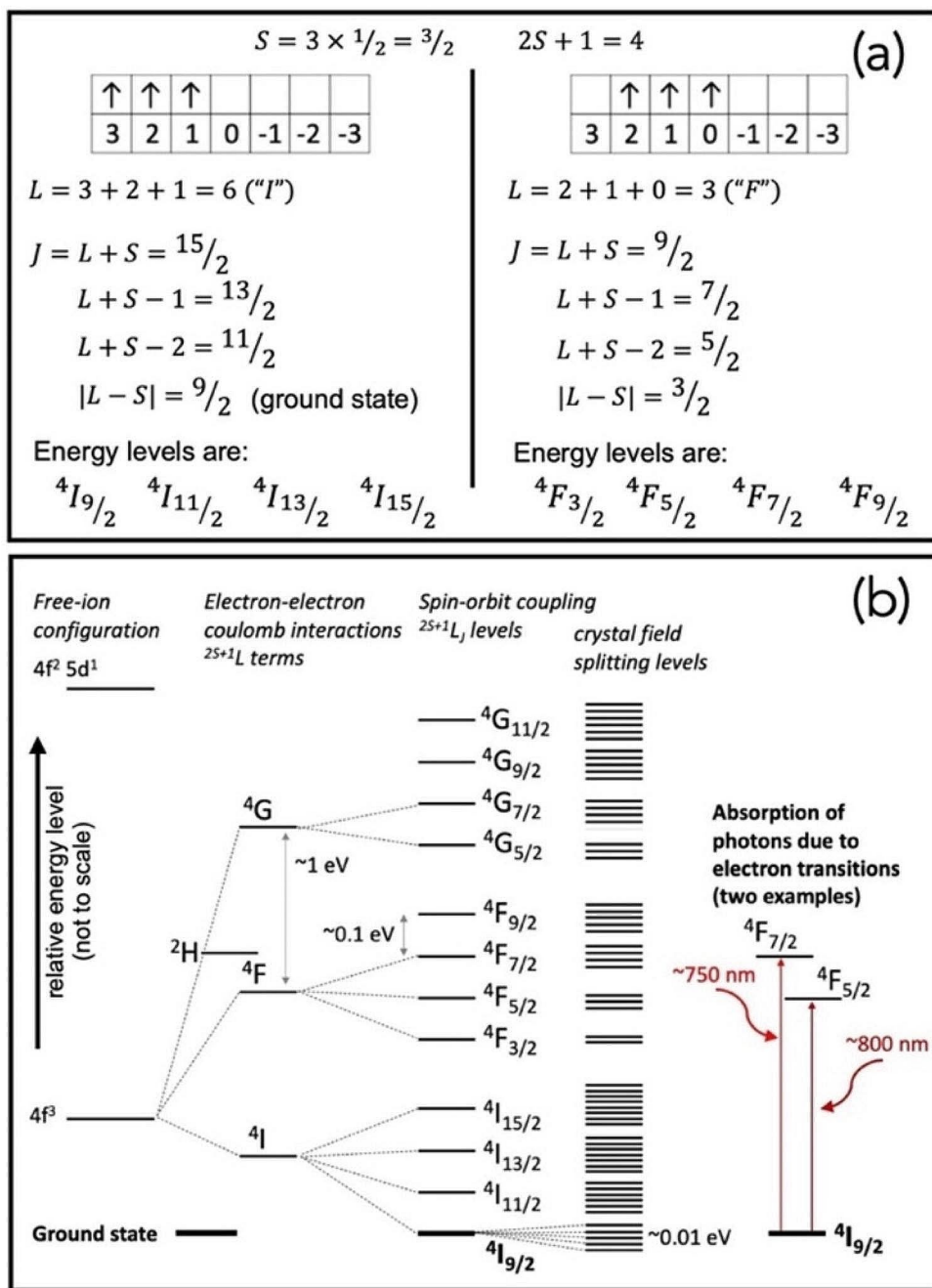
Deggendorf, Germany, with reported > 99.9% purity; La_2O_3 was purchased from Merck, also with reported > 99.9% purity. These oxide powders were dried at 105 °C for at least an hour before weighing out desired masses. In the case of cerium, Ce(III) phosphate powder was purchased directly (Alfa Aesar/Thermo Scientific, 99% purity), characterized by us as having the rhabdophane structure by means of X-ray powder diffraction (XRD). The general approach was that a total amount of 5.0 mmol of rare earth elements were weighed out and dissolved in 27 ml concentrated orthophosphoric acid (H_3PO_4, Merck Emsure for analysis, 85%), and 5 ml ultrapure water (Millipore, resistivity > 18.2 MΩ·cm at 25 °C) to reduce the viscosity. It took anywhere between 15 min and 2 h to fully dissolve the oxide powders in the acid with continuous stirring, and the HREE typically needed a heating to 50–60 °C to fully dissolve. The solutions were then made up to 210 ml with ultrapure water in 250 ml borosilicate glass beakers covered with a watch glass. The solution was stirred with a magnetic stirrer and brought to a vigorous boil on a hotplate, and left boiling

for 1.5–2 h. This led to the precipitation of hydrated REE-phosphates. The suspension was then filtered by means of a 2 μm filter paper and the material retained in the filter was washed with ultrapure water until the liquid passing through the filter had a neutral pH. The powder collected within the filter paper was then left to dry at room temperature in the fume hood overnight. The dried precipitate was weighed, and analysed by X-ray powder diffraction. Small aliquots of some of these precipitates were subjected to thermogravimetric analysis. Subsequently, the synthesized powders, as well as the purchased Ce(III) phosphate, were transferred to porcelain crucibles and heated for 6 h to 800 °C (for the LREE: La to Gd) or 900 °C (HREE: Dy to Lu, and Y) in a conventional muffle furnace in static air atmosphere. Testing had shown that heated HREE-phosphates formed xenotime rather than monazite, but required a higher temperature for a complete transformation from the hydrated precursor REE-phosphate. The resulting powders were analysed by XRD, and their reflectance spectra were collected by a 350–2500 nm field spectrometer. The effects of the rare earth elements Tb and Ho were not studied; they have a very low abundance in nature, and their oxides were prohibitively expensive at the time of our experiments.

Following this general approach we prepared three groups of synthetic phosphate compounds. Firstly, we made single-REE monazites and xenotimes. Secondly, because the synthesis of phosphates of HREE yielded the mineral xenotime after heating, we also synthesized HREE-doped monazite-(La) (e.g., $LaPO_4$:Dy in materials science parlance), containing La, and one of the group Dy, Er, Tm, Yb, Lu, Y, in a 95:5 molar ratio. The idea behind this experiment was that trivalent La does not show absorption features due to spin-orbit coupling or crystal field electronic processes as a result of its $4f^0$ electronic configuration, hence we mainly expect to see the absorption features due to the trivalent HREE 'dopant' in the solid solution. In this experiment, the HREE and La oxides (a total of 5.0 mmol REE) were each dissolved separately in concentrated phosphoric acid (total 27 ml) with a few ml of ultrapure water with continuous stirring; the HREE solutions needed to be heated to 50–60 °C to fully dissolve. The solutions were poured together in a 250 ml beaker, made up to 210 ml with ultrapure water, and brought to the boil. Thirdly, a 'natural-like' multi-REE monazite was synthesized that contained lanthanum plus four spectrally active, naturally-abundant lanthanides (La, Pr, Nd, Sm, Dy). Ce was omitted from this experiment because the monazite-(Ce) showed no absorption features in the studied wavelength range (see below), and we wished to avoid the complication of having tetravalent Ce in this monazite; the effect of Ce^{4+} was investigated separately (see next paragraph). Oxide masses corresponding to 3.4 mmol La, 0.30 mmol Pr, 0.90 mmol Nd, 0.30 mmol Sm

and 0.10 mmol Dy (total 5.0 mmol lanthanide ions) were weighed out, dissolved together, and synthesized into monazite. The relative molar abundances of Pr, Nd, Sm and Dy were informed by those in natural monazite, and, assuming no fractionation during synthesis, would make a monazite with a $(La_{0.68},Pr_{0.06},Nd_{0.18},Sm_{0.06},Dy_{0.02})PO_4$ homogeneous composition.

To investigate the spectroscopic effect of tetravalent Ce in monazite, 5.0 mmol of pre-prepared synthetic monazite-(Ce) powder was combined with an oxidizing solution containing 0.050 mmol $KMnO_4$ in 250 ml ultrapure water, stirred for 1.5 h at 80 °C. Within minutes the pink solution turned colourless due to the reduction of Mn^{7+} to Mn^{2+}, and the off-white monazite-(Ce) powder turned brick-red brown, as a maximum of 5% of the present Ce^{3+} was oxidized to Ce^{4+} (assuming that 1 mol of Mn^{7+} can oxidize at most 5 mol of Ce^{3+} to Ce^{4+}). In the resulting oxidized monazite, the presence of Ce^{4+} was most likely compensated by structural defects such as vacancies in cation sites, as testing showed that this powder lost its brown colour again after heating to 800 °C for 6 h in air. Nonetheless, this experiment gave us an insight in the nature of the brown colour of natural monazite.

To investigate the spectral expression of different ligands and coordination symmetries on the Nd ion, we put together a series of synthetic Nd-bearing phases. This included the Nd-oxide powder used for synthesis (Nd_2O_3) without additional treatment, and rhabdophane-(Nd) from the single-lanthanide monazite synthesis experiment but without the subsequent heating step to monazite-(Nd). Moreover, $NdCl_3$ hydrate was prepared by evaporating a solution of Nd_2O_3 dissolved in HCl (molar Nd: Cl = 1:3) to dryness. A synthetic variety of the mineral fluocerite-(La), i.e., Nd-doped LaF_3 (i.e., $(La, Nd)F_3$) was prepared by precipitation from a solution of $La(NO_3)_3 \cdot 6H_2O$ and $Nd(NO_3)_3 \cdot 6H_2O$ (La: Nd = 9:1) and excess NaF (F: (La + Nd) ~ 4:1), stirred for 4 h at 70 °C. Finally, a Nd-carbonate (kozoite-(Nd), $NdCO_3(OH)$) was prepared by precipitation from a Nd-chloride solution by adding a solution of dissolved Na_2CO_3 (molar Nd: CO_3 = 1:1).

Crystallographic and spectroscopic analytical methods

The synthesized mineral powders of all above experiments were analysed by X-ray powder diffraction (XRD) in a Bruker D2 Phaser instrument with a Cu X-ray source. The powders were lightly milled by hand in an agate pestle and mortar to break up the larger crystal powder aggregates. Powders were placed in a standard Bruker sample holder and gently compacted and levelled with a glass plate. Integration of 10 or more scans with a 2θ range from 6 to 80°

Fig. 3 (a) X-ray powder diffractograms for synthesized phosphates after heating. Single-lanthanide synthetic phosphates of La to Gd transformed to monazite (mnz). Single-lanthanide synthetic phosphates of Dy to Lu and Y transformed to xenotime (xnt). Diffractograms of natural monazite from our collection and of a synthesized 'natural-like' mixed-lanthanide monazite are also shown. Stick diagrams of crystallographic reference data of monazite-(La) and xenotime-(Y) are shown for comparison. Note the systematic shift to higher 2ϑ angles (smaller d-spacings) from La to Gd in monazites, and from Dy to Lu in xenotimes
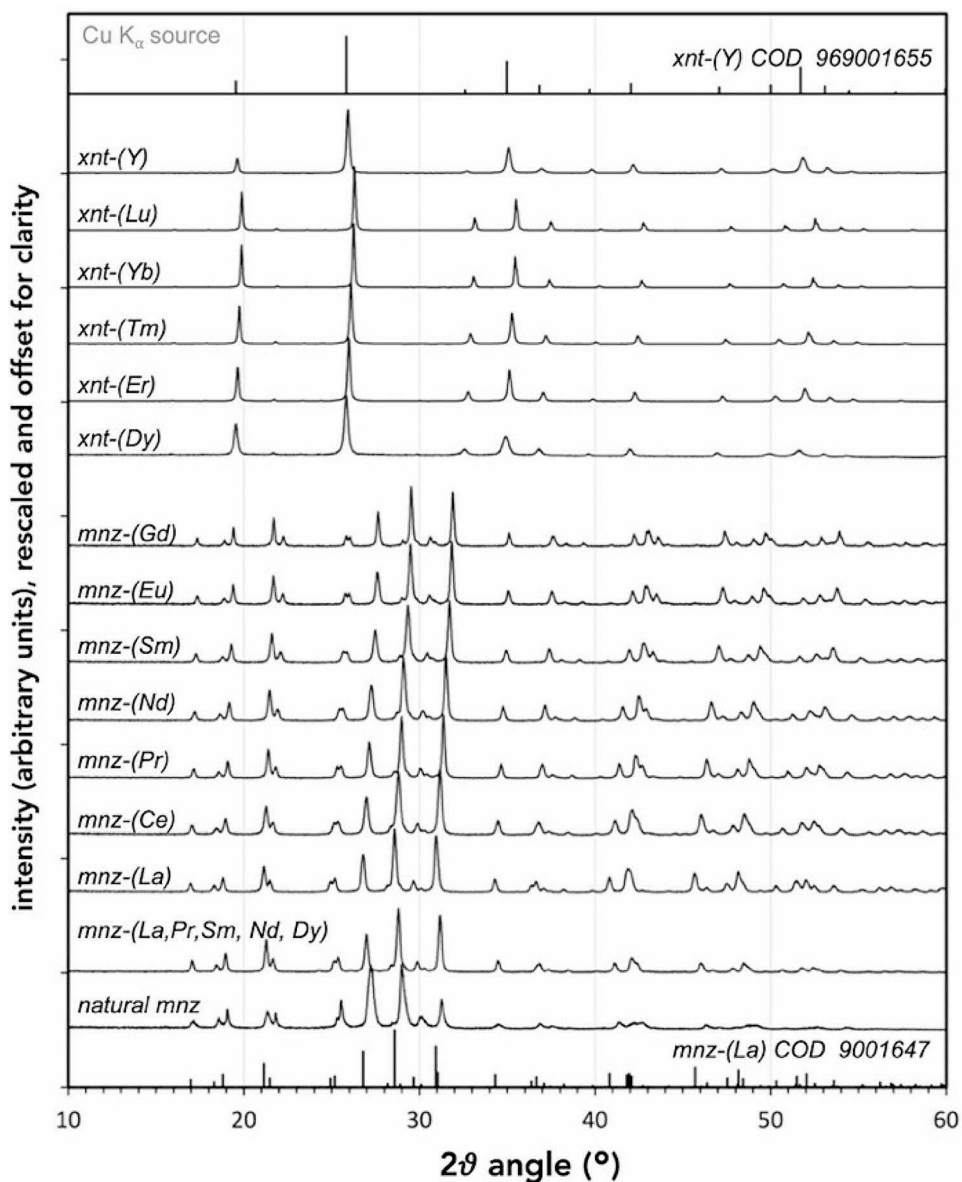
with a step size of 0.012°, time step of 0.1 s, source slit of 0.6 mm, knife of 1 mm and detector slit of 8 mm were used, giving a typical total run time of 109 min per analysis. Structural refinement was carried out with the MAUD package, version 2.9993 (Lutterotti et al. 2007), using the crystallographic data from Ni et al. (1995) found in crystallographic information files 9,001,646 ($CePO_4$ monazite), 9,001,653 ($GdPO_4$ monazite), 9,001,654 (YPO_4 xenotime), and 9,001,661 ($LuPO_4$ xenotime) from the Crystallography Open Database (2023). Discrepancies between measured and fitted diffraction data for the 2θ range 15–60° of the synthetic single-REE phases, as measured by the weighted profile R-factor (R_{wp}%), were between 5.3 and 9.8.

Thermogravimetric analyses (TGA) were carried out on selected synthesized powders by means of a Perkin Elmer

8000 instrument. Circa 0.025 g of sample powder was held at 40 °C for 2 min, then heated from 40° to 105 °C with a temperature increase of 30 °C/min, held at 105 °C for 5 min, and then heated to 900° C (10 °C/min) and held at 900 °C for 10 min; all steps were carried out under a N_2 flow of 40 ml/min.

Reflectance spectra encompassing the 350 to 2500 nm wavelength range were obtained with an ASD Fieldspec 3 instrument. An uncovered 40 mm diameter circular quartz glass plate loaded with c. 1 g of compacted sample powder in a 1.5–2 mm thick layer with a diameter of 30–35 mm was illuminated by a 70 W ASD 'Illuminator' quartz-tungsten-halogen lamp with an incident angle of c. 60°, and the reflectance spectra were recorded with a pistol grip attachment (25° field of view, full conical angle) mounted in a

laboratory clamp connected to the spectrometer by means of a fibre-optic cable. The distance between the sample powder and the pistol grip lens was consistently kept at 60 mm. A 100% white-standard plate (Spectralon™) was measured before every sample to allow measured intensity of radiant energy to be converted to reflectance values between 0 and 1. The spectral resolution of the instrument, as reported by the manufacturer, is 3 nm at 700 nm, and 10 nm at 1400 and 2100 nm (full width at half maximum), with a sampling interval of 1 nm. As a quality control measure, reflection spectra of a sheet of Mylar (NIST SRM-1920a), and of a natural ruby crystal with the characteristic emission at 695 nm, were obtained alongside the samples. It was found that the accuracy of the wavelength of the absorption features was better than 1.5 nm across the entire wavelength range used.

Results

Precipitation products

The colour of the synthesized powders in natural light was generally colourless or slightly off-white. However, the phosphate of Pr was pale green, the phosphate of Nd pale pink, and the phosphates of Ce and Sm had yellow hues.

X-ray powder diffraction showed that the precipitation products of the experiments of La, Pr, Nd, Sm, Eu and Gd had the structure of the hydrous REE-phosphate rhabdophane. The purchased powder of $CePO_4$ was also determined to have rhabdophane structure. The thermogravimetric analysis of three representative products (La, Nd and Gd) from our LREE experiments (see supplementary information, SI-Fig. 1) showed that the powders gradually lost mass between 40 and 105 °C depending on their initial state of dryness (e.g., presence of absorbed water), and that they quickly lost most of their structurally-bound water (3–4 wt%) between 160 °C and 260 °C, followed by a gradual mass loss c. 1% between 260 °C and 900 °C. Calculated n values (moles water per mol lanthanide phosphate) at 105 °C in $[REE]PO_4 \cdot nH_2O$ are 0.68, 0.71 and 0.64 for [Ln]=La, Nd and Gd respectively, and 0.15, 0.12 and 0.12 after the steep mass loss at 160–260 °C. In an additional test, XRD results of $NdPO_4 \cdot nH_2O$ powders heated to different temperatures revealed that rhabdophane-(Nd) was the stable phase at temperatures up to c. 650 °C; heating for 2 h at 700 °C already yielded monazite-(Nd) as the only phase, although the peaks in the XRD diffractograms were broader and less well defined than those for the products of heating to 800 °C for 6 h.

XRD analysis showed that the products of the precipitation step of the synthesis using the HREE Dy, Er, Tm, Yb,

Lu, and Y were mixtures of rhabdophane and churchite. Upon heating in the muffle furnace for 6 h at 800 °C, the phases recrystallized to anhydrous xenotime. It was found, however, that a temperature of 900 °C was needed for a full transformation. The experiments aimed to make HREE-doped monazite-(La) as well as multi-element monazite all initially yielded rhabdophane as the only precipitated phase, which also successfully recrystallized to monazite after heating.

Calculated effective yields (moles of the lanthanide in the product vs. moles of the lanthanide in the dissolved oxide powder) for all the experiments based on the masses of the heated, fully dehydrated products were 50 to 99%. In some of the (early) experiments, boiling time were probably not sufficient to form the phosphate precipitates, or not all precipitated particles were retained on the filter. In later experiments, vigorous boiling for > 1.5–2 h was maintained, which routinely gave yields of 90–99%. The yields for the doped monazites and for the multi-element monazite were > 87%, precluding large fractionation between REE proportions in the solutions and in the bulk synthetic crystalline products. However, this does not rule out the formation of internally zoned crystals or compositional differences between early- and late-formed crystals due to fractionation of the REE during crystallization.

Single-REE monazites and xenotimes

After heating to 800 °C, all the La, Ce, Pr, Nd, Sm, Eu and Gd synthesized products had fully transformed to a monazite structure (Fig. 3). There is a systematic shift of the monazite peaks in the XRD diffractograms to higher 2θ angles (i.e., smaller d-spacings) with increasing atomic mass, as expected considering the decreasing ionic radii associated with the lanthanide contraction. Structural refinement results showed a linear decrease in unit cell dimensions, and an increase in the β angle from 103.3 to 104.0°, with decreasing ionic radii (Fig. 4); the measured values and trend match the results of the high-resolution structural monazite study of Ni et al. (1995) with an acceptable level of accuracy: relative deviations of unit cell dimensions were < 0.16% (mean 0.12%).

The heating to 900 °C of the precipitated phosphates of Dy, Er, Tm, Yb, Lu and Y produced high-purity xenotime (Fig. 3). Here we also observe a shift of the main peaks in the diffractograms to higher 2θ values with increasing atomic mass, from Dy to Lu; the peaks of Y are positioned between those of Dy and Er (almost certainly between Dy and Ho if Ho had been included in our study). The refinement results show the tetragonal nature of xenotime (Fig. 4). Again, the measured unit cell parameters match those of the study of
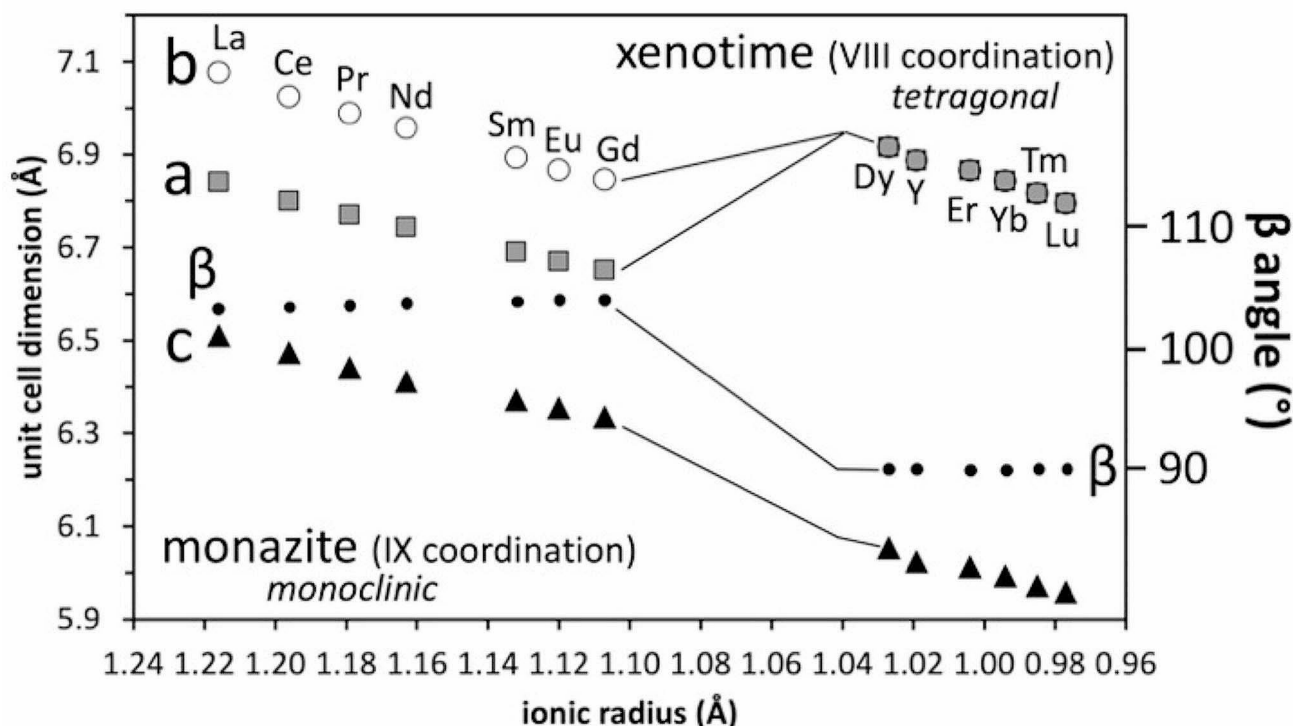
Fig. 4 Results of the structural refinement of the X-ray diffraction data of synthesized monazite and xenotime, showing the systematic decrease of unit cell dimensions a, b, c with decreasing ionic radius of the lanthanides from La to Lu (lanthanide contraction), and the switch from monoclinic ($\beta \approx 103$–$104°$) monazite to tetragonal ($a = b > c$, $\beta = 90°$) xenotime. Ionic radii of trivalent La to Gd are for 9-fold coordinated lanthanides; radii of trivalent Dy to Lu and Y are for an 8-fold coordination (Shannon 1976)

Ni et al. (1995): relative deviations of unit cell dimensions were < 0.27% (mean 0.18%).

The reflectance spectra from 350 to 2500 nm of the synthesized single-REE monazites and xenotimes are presented in Fig. 5. These spectra, and the observed absorption features, are discussed below.

HREE-doped monazite-(La)

XRD diffractograms of heated La phosphates with a c. 5% molar contribution of one of the HREE Dy, Er, Tm, Yb, Lu or Y are presented in the supplementary information (SI-Fig. 2a). The diffractograms show that these synthesized phases are monazite, and they are near-identical to undoped monazite-(La). Nonetheless, the very small shifts of peaks to higher 2θ angles and the absence of discernible xenotime peaks confirm that the products are HREE-La solid solutions, and not mixtures of monazite-(La) with another HREE-phase.

Reflectance spectra of the six HREE-doped monazite-(La) powders are presented in SI-Fig. 2b. The spectra of Dy-, Er-, Tm-, and Yb-doped monazite-(La) samples are shown in Fig. 6, where they are compared directly to their xenotime counterparts.

Multi-element, 'natural-like' monazite

The synthesized phosphate with La, Pr, Sm, Nd, and Dy in natural proportions is also confirmed by XRD as monazite after heating (Fig. 3). The reflectance spectrum of this monazite is presented in Fig. 7, together with that of a milled natural monazite powder from our collection.

Monazite-(Ce^{3+}) and monazite-(Ce^{3},Ce^{4+})

XRD analysis showed no discernible structural differences between the monazite-(Ce) sample before and after oxidation in a $KMnO_4$ solution. The colour change from an off-white powder with a yellow hue to a brown powder is seen also in the reflectance spectra in Fig. 7: there is a very strong drop-off in the reflectance values going towards shorter wavelengths in the Ce^{4+}-bearing sample. For instance, between 450 and 600 nm, the reflectance amounts 0.7–0.8 in the unoxidized sample, and is reduced to 0.1–0.3 in the oxidized, brown sample. This indicates that, upon oxidation, the wavelengths between 450 and 600 nm (violet – yellow) are more effectively absorbed by the sample, whereas those above 600 nm (yellow – red) are still strongly reflected; leading to the brownish colour of the sample. The general

Fig. 5 Measured reflectance spectra from 350–2500 nm for synthetic single-REE monazites and xenotimes. La, Ce, Pr, Nd, Sm, Eu and Gd phosphates are monazites, whereas Dy, Er, Tm, Yb, Lu and Y phosphates are xenotimes. Electron configurations in the 4f subshell of the trivalent REE ions are indicated on the right
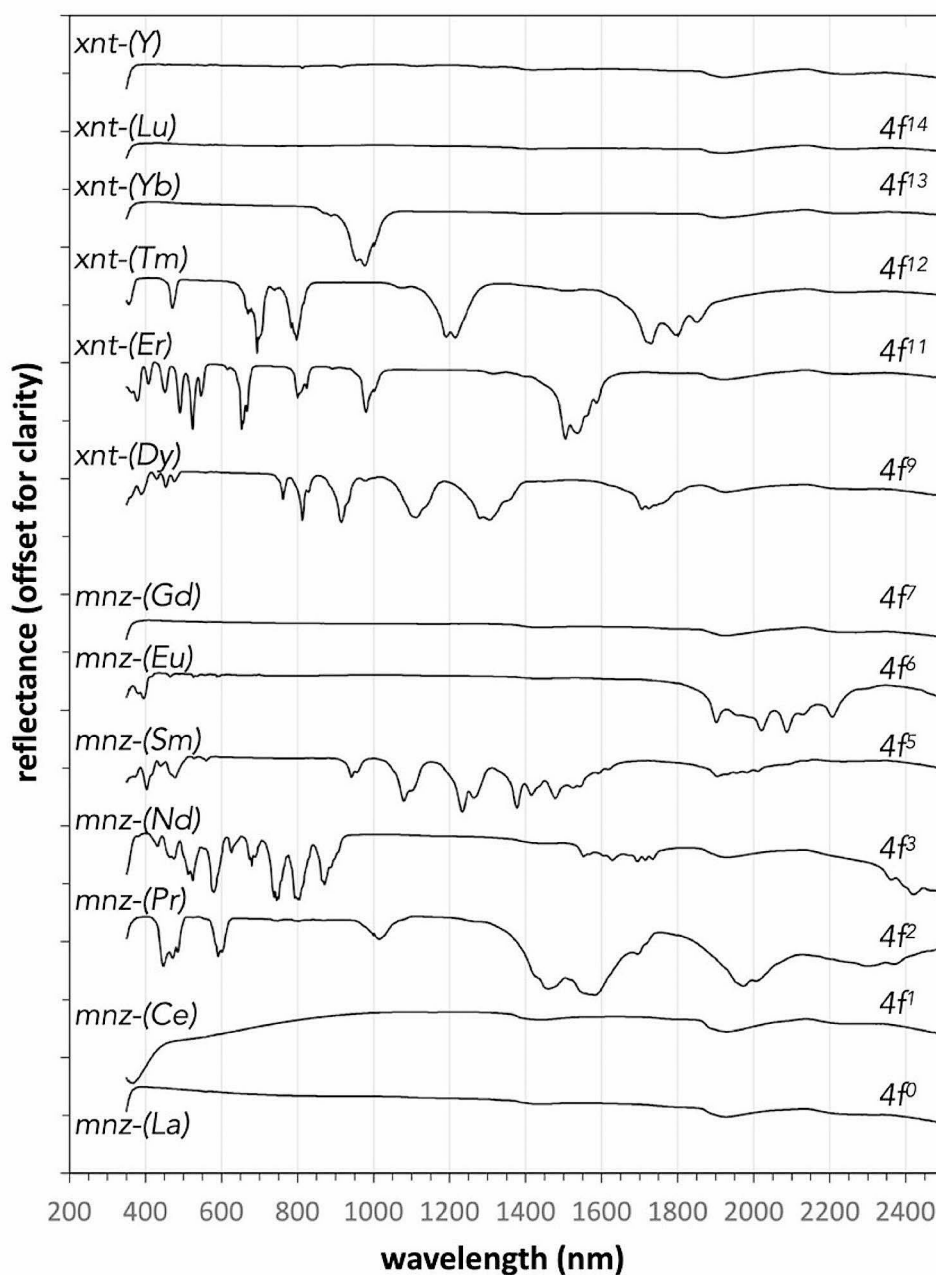

trend of the reflectance spectrum of the Ce^{4+}-bearing monazite sample also closely follows the continuum 'hull' (the shape of the reflectance curve without the discrete absorption minima) of the reflectance spectrum of natural, brown monazite powder.

Other synthesized compounds

X-ray powder diffractograms of the additional synthetic neodymium phases for comparison are provided in the supplementary information (SI-Fig. 3). The 'Nd-oxide' starting powder contains both cubic and hexagonal Nd_2O_3, and

Nd-hydroxide ($Nd(OH)_3$, peak at $2\theta = 16.0°$). The highly complex diffractogram for $NdCl_3$ hydrate, $NdCl_3 \cdot nH_2O$, shows that it is a mixture of many hydrates in addition to the common hexahydrate ($n = 6$); no attempt was made to distinguish and identify them. The Nd-carbonate is confirmed as orthorhombic kozoite-(Nd) (9-fold coordinated cation), with no other phases. The Nd-doped La-fluoride, (La, Nd)F_3, matches hexagonal fluocerite-(La), LaF_3 (11-fold coordinated cation), without any other phases; the broadness of the peaks suggest the powder consists of nanoscale crystallites. The reflectance spectra of these different Nd phases are given in Fig. 8 and are discussed below.

Fig. 6 Comparison between reflectance spectra of xenotime-(HREE) shown as grey curves, and monazite-(La) doped with the same REE (where molar HREE/(La + HREE) is c. 5%) shown as black curves. There is a strong effect of the much lower concentrations of the spectrally active HREE in the doped monazites, expressed as a reduced depth of the absorption features. The splitting of the absorption features into multiplets, corresponding to the Stark levels due to splitting of the energy levels under the influence of the crystal field, is also much more clearly expressed in the xenotime powders. It is also noteworthy that well-defined absorption features at wavelength > 1600 nm in the xenotimes of Dy and Tm are not observed in the corresponding Dy and Tm-doped monazites
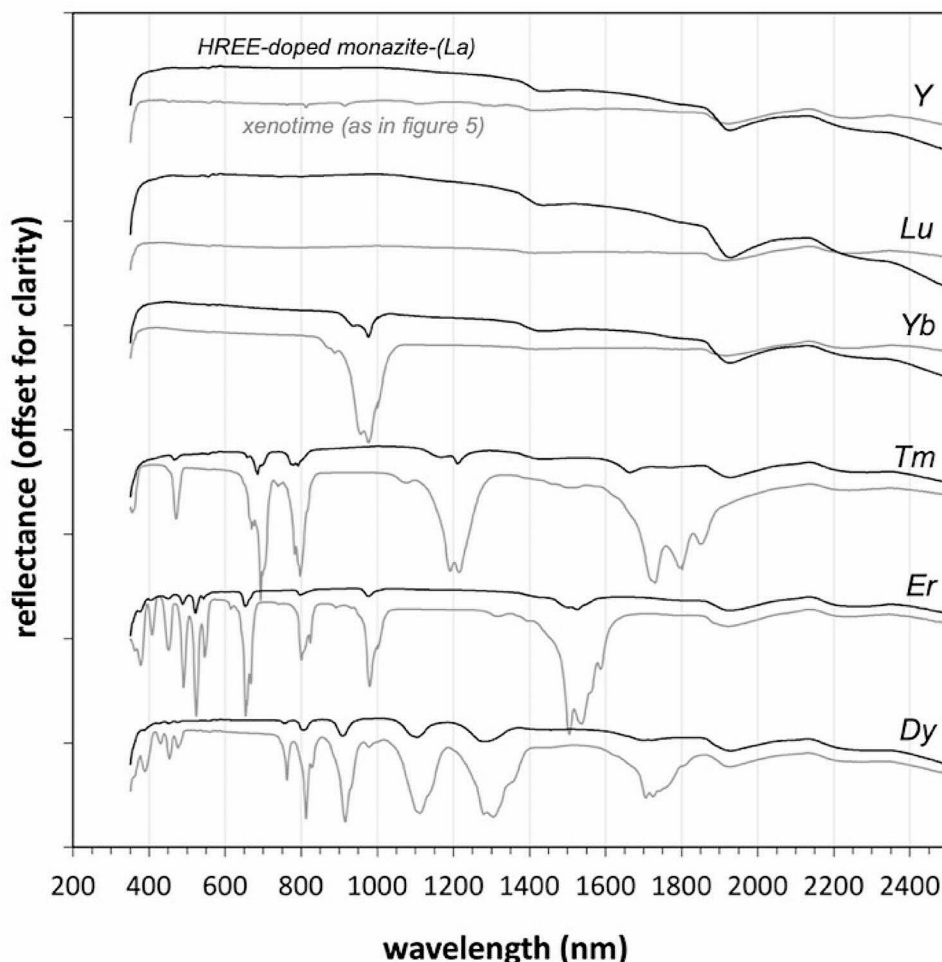
Discussion

Synthesis

As shown by the results presented above, the described synthesis – consisting of hydrous precipitation followed by dehydration and recrystallisation at 800–900 °C - yielded single-phase monazite and xenotime. We were also successful in synthesizing HREE-doped monazite-(La) with 5% molar HREE in solid-solution with La, and a multi-element monazite by the same approach. Therefore, there can be little doubt that the reflectance spectra obtained are representative for the minerals monazite and xenotime, and that our results and analysis will have significant relevance for the spectroscopic study of their natural counterparts.

Reflectance Spectra of single-REE monazite and xenotime

As Fig. 5 shows, individual single-REE monazites and xenotimes have distinctly different reflectance spectra in the

studied wavelength range, in combination with a set of common features.

A common feature is the steep drop-off of reflectance values resembling the start of an absorption edge at wavelengths below 400 nm, at the lower end of the studied wavelength range. Absorptions due to f-d electron transitions are typically observed well into the UV domain, and also cannot explain the drop-off in monazite-(La) and xenotime-(Y) seen in Fig. 5, given the absence of 4f electrons in the La^{3+} and Y^{3+} ions. Kumar et al. (2022) report valence-to-conduction-band transfer-related optical bands gaps in monazite-type La-Nd phosphates with energies of 3.45–3.58 eV, which agree well with the observed absorption features at the high-energy, short-wavelength part of the reflectance spectra of our synthesized monazites and xenotimes.

Another common feature is the presence of broad, shallow absorptions at 1925–1930 nm (depth < 10%) and 2223–2224 nm (< 5%). These are best observed in the spectra of La, Ce, Nd and Gd monazite, and in Dy, Er, Yb, Lu and Y xenotime (Fig. 5). They are also seen in the spectra of HREE-doped monazite-(La) in Fig. 6. In the monazites of Pr,
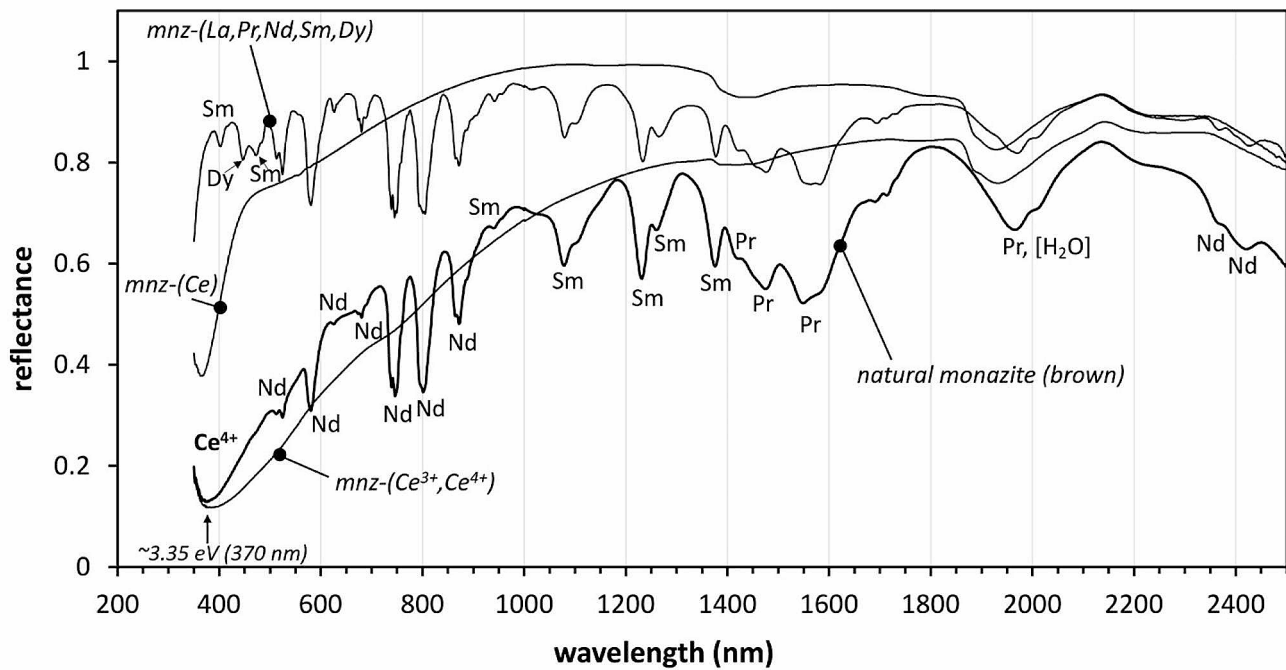
Fig. 7 Reflectance spectrum for natural, brown monazite powder (bold curve), compared with synthesized, 'natural-like' monazite-(La, Pr, Nd, Sm, Dy), synthesized monazite-(Ce), and oxidized monazite-(Ce^{3+},Ce^{4+}). The absorption features in the natural monazite are labeled with the main lanthanide causing the absorption, based on the reflectance spectra of the single-lanthanide monazites. The marked drop in albedo towards short wavelength observed in natural monazite, with a local minimum near 370 nm and an overall low albedo at wavelengths < 600 nm causing the brown colour, is reproduced in the synthesized Ce^{4+}-bearing monazite (see discussion about the possible role of the O$_{2p}$-Ce$_{4f}$ charge-transfer process)
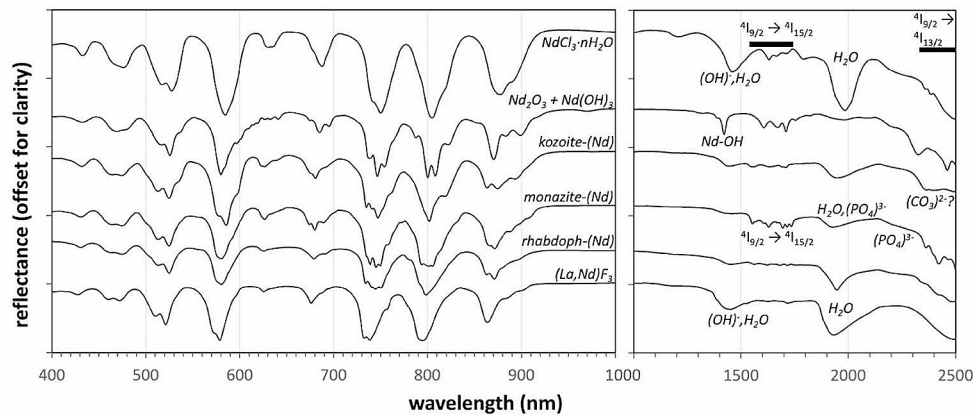

Fig. 8 Reflectance spectra of six synthesized neodymium compounds, offset for clarity: Nd-doped lanthanumfluoride; rhabdophane-(Nd), monazite-(Nd); kozoite-(Nd), a NdCO$_3$(OH) carbonate; Nd-oxide; and Nd-chloride hydrate. Note the different wavelength scales for the left-hand panel (400–1000 nm range) and right-hand panel (1000–2500 nm range). The absorption features seen in the < 1000 nm range, which are due to electronic transitions in the shielded 4f orbitals in the Nd^{3+} ion, are to a first order very similar. However, there are also clear differences between the spectra, which can be attributed to the effects of the nature of the ligands and their bonds to Nd, and of the crystal field. The spectra in the > 1000 nm range include absorption features due to electronic processes (marked) as well as expected absorption features resulting from vibrational processes in bonds of the [OH]$^-$, [PO$_4$]$^{3-}$, and [CO$_3$]$^{2-}$ functional groups and in H$_2$O. See text for discussion

Sm and Eu, and in xenotime-(Tm), they are partly obscured by much more prominent electronic absorption features. Given their presence in all the synthesized monazites and xenotimes, these features are attributed to overtones and/or combinations of vibrational modes in the [PO$_4$]$^{3-}$ functional group (Hunt 1977).

The remaining absorptions that can be observed in the single-lanthanide monazites of Pr, Sm, Nd, and Eu, and xenotimes of Dy, Er, Tm and Yb are all unique in terms of

their wavelength positions, depths and shapes. They tend to be relatively sharp (≤ 50 nm wide), especially in the visible and near-infrared; it can be seen that they typically consist of multiple narrower absorption features, so-called multiplets, ≤ 10 nm wide. Lanthanide monazites with empty (La^{3+}, $4f^0$) or half-filled (Gd^{3+}, $4f^7$) 4f subshells do not show any strong absorption features other than the common features discussed above. The same is observed for Lu^{3+} ($4f^{14}$, i.e., fully filled 4f subshell), and for Y^{3+} (no 4f subshell) in the xenotimes or HREE-doped monazites. Spin-forbidden transitions associated with high-energy, UV photons (< 310 nm) are known for Gd^{3+} compounds (e.g., Carnall et al. 1978), but are outside of the studied wavelength domain. Note that there are very minor absorptions (depth of the absorption ≤ 0.02 in reflectance values) visible in the xenotime-(Y) spectrum at the same wavelengths as the strong absorptions in xenotime-(Dy), suggesting that the Y_2O_3 starting oxide contained some Dy_2O_3 or that some contamination occurred during synthesis. For Ce^{3+} ($4f^1$), no electronic transitions are observed in the studied wavelength range; the data for Ce^{3+} in fluoride from Carnall et al. (1978) indicate that absorptions due to intra-configurational 4f-4f transitions occur at wavelengths > 3500 nm.

In Fig. 9, we have shown the example of the measured monazite-(Nd) reflectance spectrum together with the absorption wavelengths corresponding to transitions from the grou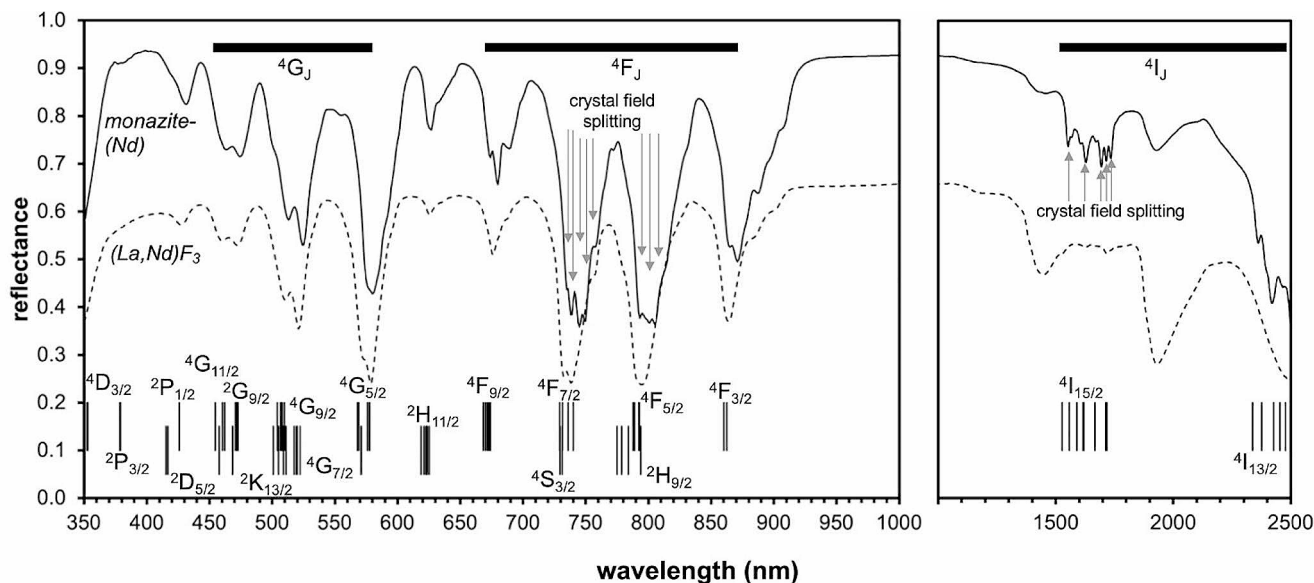nd state to the higher energy spin-orbit coupling energy levels of the Nd^{3+} ion in Nd-doped LaF_3 from the study of Carnall et al. (1978). The wavelength positions and the spacing between the absorption features agree well. The effect of the crystal field, i.e., the influence that the ligands and their coordination exert on the energy levels within the shielded 4f subshell can be seen in the splitting of the absorption features into narrow multiplets, corresponding to the crystal field splitting levels. These multiplets are 5–10 nm wide in the visible and near-infrared domain, and somewhat wider, 15–20 nm at higher wavelengths. It is noted that the measured absorption features in the synthesized monazite-(Nd) occur at ~ 10 nm longer wavelengths (lower energies) compared to those from the Carnall et al. (1978) study. This shift exceeds the wavelength accuracy of our spectrometer and is probably an effect of the different ligands (e.g., F^- is more electronegative than O^{2-}). This is supported by the observation that the absorption features in our own synthesized Nd-doped LaF_3 shown in Fig. 9 are also shifted to lower wavelengths compared to those in monazite-(Nd), albeit not as much as in the Carnall et al. (1978) data. The topic of the wavelength shift of the spin-orbit coupling related features is discussed below.

Fig. 9 Annotated reflectance spectrum for synthetic monazite-(Nd). Note the different wavelength scales for the left-hand panel (visible and near infrared, 350–1000 nm range) and right-hand panel (1000–2500 nm range). Absorption features are interpreted as resulting from electronic transitions from the ground state ($^4I_{9/2}$) to higher energy levels associated with spin-orbit coupling; marked transitions are taken from the study of Carnall et al. (1978) measured on Nd-doped lanthanum trifluoride; some markers are offset vertically for clarity. The reflectance spectrum of the Nd-doped lanthanum trifluoride synthesized in our study is shown for comparison (dashed line labeled (La, Nd)F_3; reflectance values offset for clarity). Several complex absorption features can be seen in the monazite which consist of c. 5–10 nm-wide multiplets in the visible and near-infrared domain (c. 15–20 nm wide in the > 1000 nm domain) which result from further splitting of the energy levels due to crystal field effects

Synthetic xenotime and HREE-doped monazite compared

When the reflectance spectra of the HREE-doped monazite-(La) powders are compared with the corresponding xenotimes (Fig. 6), a strong effect of the difference in concentration of the spectrally active HREE's Dy, Er, Tm and Yb can be seen as a much-reduced depth of the absorptions in the monazites. The splitting of the absorption features into multiplets is also much more clearly expressed in the xenotimes. The direct comparison also reveals that well-defined and relatively deep absorption features at wavelengths > 1600 nm, both in xenotime-(Dy) and xenotime-(Tm), seem to be absent in the corresponding Dy- and Tm-doped monazites. This suggests that the difference in the crystal field experienced by the REE cation in monazite and xenotime, primarily the different coordination and REE-oxygen bond length and strength, also strongly affects the depth of spin-orbit coupling related absorption features.

A comparison to natural monazite

In natural monazite, the LREE are much more abundant than the HREE. Our mixed-REE synthetic monazite with bulk composition $(La_{0.68},Pr_{0.06},Nd_{0.18},Sm_{0.06},Dy_{0.02})PO_4$ (quoted molar proportions assume that no significant fractionation occurred during synthesis) contained the four most abundant lanthanides found in natural monazite with absorption features in the studied wavelength range (Pr, Nd, Sm, Dy) in 'natural-like' abundances. These four elements are in solid-solution with La (as confirmed by XRD, Fig. 2 in supplementary information), which lacks spin-orbit coupling absorption features in the studied range. As seen in Fig. 7, this produced a monazite with absorption features at identical wavelengths, and with similar depths and shapes, as those found in the natural monazite from our collection measured alongside the synthetic sample. From the comparison it is obvious that the absorptions in natural monazite are dominated by those of Nd, Sm and Pr. While the Nd absorptions dominate the visible and near-infrared part of the spectrum, those of Sm and Pr dominate the spectrum between 1000 and 1600 nm. There are no significant absorption features in the natural monazite that are not also present in our synthetic monazite-(La, Pr, Nd, Sm, Dy). However, the absorption features at wavelengths < 500 nm seen in the synthetic monazite are not seen in the natural monazite, due to the sharp drop-off in reflectance of the natural monazite at decreasing wavelengths; as a result, the only absorption that can be attributed to the presence of Dy, near 455 nm, is no longer visible in the natural sample. Interestingly, an absorption feature at this wavelength can be observed in the natural monazite (4) from the Siglo Veinte mine in Bolivia in Fig. 1.

The implications of this are that only Pr, Nd and Sm are detectable REE in natural monazite using reflectance spectroscopic techniques. Conversely, the absorptions due to Nd can be used in the visible and near-infrared range, while the absorption resulting from Pr and Sm (despite their low abundances) can be used in the shortwave infrared range, to detect REE-bearing minerals such as monazite using (imaging) reflectance spectroscopy techniques. Based on the analysis in Fig. 7 we can define the most diagnostic absorption features for the trivalent ions of Nd, Sm and Pr in monazite. These absorptions should be relatively deep, have the least amount of interference with those of other REE ions (including Ce^{4+}) and should not have wavelength near those of the well-known broad absorption features caused by vibrational processes in the OH and/or H_2O molecules at 1400 and 1900 nm. The absorptions thus deemed diagnostic are at wavelengths 580, 745, 800 and 870 nm for Nd; at 1080 and 1235 nm for Sm; and at 1570 nm for Pr.

The effect of Ce^{4+} in monazite

Natural monazite shows a gradual drop-off of reflectance values (albedo) with decreasing wavelengths < 900 nm, which is associated with the brown colour. Nasdala et al. (2020) showed that metamictisation, the partial destruction of the crystal lattice due to radiation, which is often reflected in darkening of minerals, is not common in natural brown monazites. To investigate the cause for the reflectance drop and colouring, we prepared an oxidized monazite-(Ce) containing Ce^{4+} in addition to Ce^{3+}. The off-white monazite-(Ce) acquired a brown colour during the oxidation, similar to natural monazite. Figure 7 shows the change in reflectance values with decreasing wavelength as a result of the introduction of Ce^{4+}. The similarity of the shape of the reflectance spectrum compared to the continuum hull of natural monazite suggests that the presence of Ce^{4+} plays a role in the reflectance drop-off at short wavelengths causing the brown colour of natural monazite.
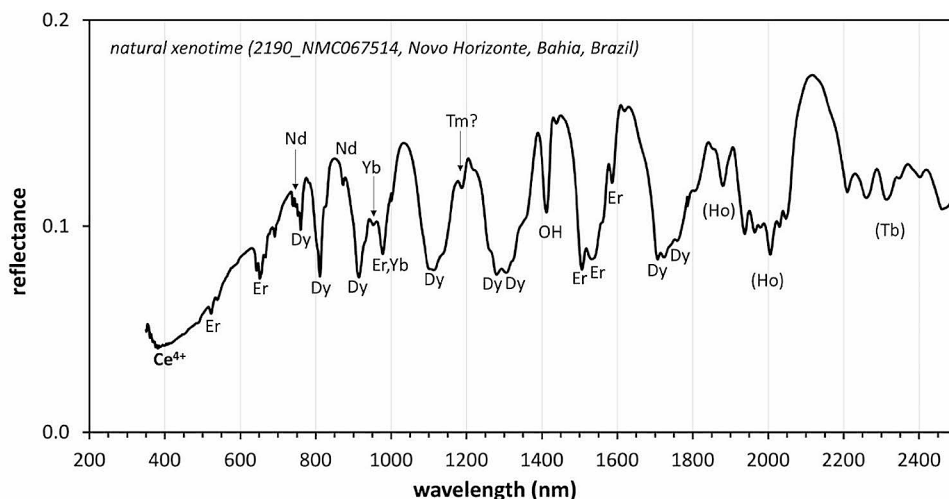
If the Ce^{4+} is hosted in the monazite structure, unbalanced by any divalent ions, this would require charge compensation probably (partly) accommodated by structural defects such as cation vacancies. It is likely that the oxidation process in our experiment introduced mainly Ce^{4+} and defects near the surface of the crystals, so surface-bound O^{2-} or OH^- anions could also play a role in locally balancing the charge. Alternatively, the Ce^{4+} in partly oxidized monazite could be hosted in another phase not easily detected by XRD (cf. van Schaik et al. 1993), for instance, $Ce_3(PO_4)_4$ (Borhan et al. 2010). One of the probable causes for the absorption at low wavelengths in the visible part of the spectrum is

a ligand to metal charge-transfer process, where an electron from an oxygen 2p orbital is transferred to a cerium 4f orbital with the absorption of a photon. In defect-bearing ceria (Ce(IV) oxide), a much-studied photocatalyst, a Ce 4f band is present between the O 2p valence band and the Ce 5d conduction band, and the O 2p to Ce 4f excitation of an electron has a band gap of c. 3.0-3.2 eV; this causes a strong absorption edge at a wavelength of c. $390-370$ nm (Yang et al. 2017; Du et al. 2020). However, this charge-transfer mechanism does not fully explain the reduction of reflectance values extending to 900 nm, which is the main cause for the brown colouration. It has been proposed that intervalence Ce^{4+}-Ce^{3+} charge transfer processes in partly oxidized cerium-compounds produce broad absorptions extending to long wavelengths, as far as 1000 nm (van Schaik et al. 1993; Griffiths et al. 1994); if the Ce^{4+} is hosted within the monazite structure together with Ce^{3+} this could perhaps be a viable colouring mechanism in monazite. It is also possible that cation vacancies or Ce^{4+} site electron holes produce colour centres affecting wavelengths 400–900 nm. This would be supported by the observation that the brown colour disappeared after heating to 800 °C in air for 6 h. In conclusion, based on this experiment we cautiously hypothesize that the cause of the brown colour of natural monazite and the overall shape of the continuum hull with a drop-off of albedo in the low-wavelength part of the visible spectrum is a function of the relative concentration of Ce^{4+}; as such, it could therefore carry information about redox processes during or after crystallization of the mineral in rocks. We note, however, this is by no means the final word on the physical-chemical cause of the brown colouring of natural monazite.

A comparison to natural xenotime

Figure 10 shows the reflectance spectrum of a natural xenotime from Novo Horizonte, Bahia, Brazil, from the GSC spectral library (spectrum (11) in Fig. 1). Like in other xenotimes, Y is the dominant REE, followed by the even-numbered heavy lanthanides Dy, Er, Yb; however, xenotimes from Novo Horizonte are also relatively enriched in the lighter lanthanides Gd and Tb compared to xenotimes from other locations (Turner et al. 2016). Using the spectra of the single-REE xenotimes and monazites, we can attribute many of the observed absorption features to individual lanthanides. We find that most of the absorption features can be attributed to the trivalent ions of Dy and Er. Low amplitude features in the visible and near-infrared are tentatively attributed to Nd. The Dy-related absorption features at 760 and 810 nm could be confused with the ~ 750 and ~ 810 nm absorptions of Nd seen in monazite. However, besides the ~ 10 nm longer wavelengths, the Dy features seem to be narrower, especially in the deepest parts, and the 810 nm feature is deeper than the 760 nm feature. The unequal depth of the 760 and 810 nm Dy features can also be observed in the natural xenotimes in Fig. 1. The single-REE xenotime spectra show that the 810 nm Dy feature also partly overlaps with absorption features resulting from Er and Tm at slightly shorter wavelength. This should mean that the depth of this feature - relative to the 760 nm feature - increases with increasing abundance of Er and Tm in a mixed-REE xenotime; in addition, the peak should become more asymmetrical, developing a shoulder at the shorter wavelength end. A feature at 975 nm can be attributed to both trivalent Er and Yb. The depth of this absorption feature with respect to other Er features can perhaps be used as an indicator for Yb enrichment in some xenotimes.

The drop-off of reflectance values going towards lower wavelengths in the visible light is not likely to be caused by the effects of Ce^{4+}, given the very low abundances of Ce^{4+} in xenotime, and remains therefore poorly understood. Interestingly, a well-defined absorption feature at 1410 nm in natural xenotime (Fig. 10, also Fig. 1) is not observed in

Fig. 10 Reflectance spectrum of a natural xenotime from the GSC Spectral Library (Percival et al. 2019). Attributions of observed absorption features to REE ions are based on the the comparison with our synthetic single-REE xenotimes and monazites. Features attributed to Ho and Tb, which are not included in the present study, are based on the spectra of oxide powders of White (1967). The sharp absorption feature at 1410 nm is interpreted as an overtone of stretching vibration in a lanthanide-bound hydroxyl group

any of the single-REE xenotimes or monazites. Below, we interpret a similarly sharp absorption feature observed in the Nd_2O_3 and La_2O_3 oxide powders at 1420 nm as an overtone of an O-H stretching vibration in lanthanide hydroxide; likewise, the 1410 nm feature in xenotime probably originates in a lanthanide-bound hydroxyl group (see also Turner et al. 2016). An absorption feature at 1875 nm followed by a broad absorption between 1900 and 2050 nm consisting of as many as 6 multiplets can almost certainly be assigned to trivalent Ho, based on the lanthanide oxide spectra presented by White (1967) and the lack of a match with any of the other lanthanides from our study. Similarly, the series of multiplets between 2200 and 2500 nm are also unmatched by our data and are probably caused by trivalent Tb based on the White (1967) study. These two lanthanides were not included in our study because of their general low abundance in minerals and their expensive nature. Ho and Tb make up only 1–2 molar% of the total REE content of xenotime from Novo Horizonte (Gysi et al. 2016; Turner et al. 2016). Despite these relatively low abundances, the spectral expressions of these elements are striking in this mineral.

Overall, we conclude that many absorption features in the near- and shortwave infrared caused by trivalent ions of Dy, Er, Ho and Tb are highly diagnostic for xenotime, and can find application in proximal and remote sensing in the future. Several strong Dy absorptions between 700 and 1350 nm, and at 1700–1800 nm are the most diagnostic in practice for proximal sensing, as they are not near H_2O or OH related absorptions frequently seen in several common minerals. The relative depth and shape of the 810 nm feature may also carry information about the abundance of Er and Tm in the sample.

Different Nd-bearing phases compared

Figure 8 shows that the reflectance spectra for several Nd-bearing phases are very similar, especially in the < 1000 nm wavelength range. The absorption features in this range, and between 1500 and 1700 nm as well as 2300–2500 nm can all be attributed to intraconfigurational 4f-4f electron excitations. The spin-orbit coupling energy levels in the 4f subshell of the lanthanide ions are largely independent of the coordination and bonding characteristics to the ligands, given that the 4f subshell is relatively shielded by the 5s and 5p subshells which extend further out in space. However, in detail, the multiplets which can be recognized within the broader absorption features, especially those at 745, 800 and 870 nm, differ in number and relative depths. The same is also true for the multiplets between 1500 and 1700 nm, which are well defined in monazite-(Nd) but less well defined or even largely absent in the other phases. As shown in Figs. 2 and 9, these multiplets are related to the

crystal field splitting levels. Theory predicts that the number of crystal field splitting levels increases with decreasing site symmetry of the lanthanide ion (e.g., Liu & Jacquier, 2006; Eliseeva and Bünzli 2010). Also the transition intensities, which should be reflected in the relative depths of the absorption features, are crystal field dependent.

Figure 8 also shows that the wavelength position of the absorption features is dependent on the nature of the ligand bonding. For instance, the wavelength median of the main absorption feature near 800 nm occurs at lower wavelength (< 800 nm) in the fluoride phase; it is located around 800 nm in the phosphate and carbonate phases (where oxygen is the main ligand for the lanthanide ion); it occurs at > 800 nm in the oxide and chloride phases. This shift to longer wavelength (i.e., lower energy) of the absorption feature is a manifestation of a shift of the spin-orbit coupling energy levels with respect to the energy level of the free ion; this shift to overall lower energies (i.e., a type of 'red shift') increases with increased covalent bonding of the anion ligands with the Nd^{3+} ion, and with larger anion polarizability, the so-called nephelauxetic, or 'cloud expanding' effect. The observed shift matches the nephelauxetic sequence of ligands that accounts for these effects (e.g., House 2020), $F < O < Cl$.

In the 1000–2500 nm wavelength range there are more prominent differences between the different Nd-bearing phases. In this domain there are typically broad (~ 100–200 nm) absorption features which are caused by overtones and combinations of vibrational modes, mainly stretching and bending vibrations, in the H_2O molecule or in $[OH]^-$, $[CO_3]^{2-}$ and $[PO_4]^{3-}$ functional groups (e.g., Hunt 1977; Clark et al. 1990). It was already noted that the synthetic monazites and xenotimes contain common absorption features at 1925–1930 nm and 2223–2224 nm associated with vibrations in $[PO_4]^{3-}$ functional groups; however, the observed relative absorption depths are low (< 0.1 reflectance value), and they are partly obscured in monazite by Pr- and Sm-related electronic absorption features occurring at similar wavelengths. In the Nd-carbonate kozoite-(Nd), a broad absorption feature centred at ~ 2355 nm corresponds to a well-known overtone of a C-O stretching mode in the carbonate group (Hunt 1977). A relatively narrow absorption feature at 1420 nm in the Nd_2O_3 oxide powder was also seen in several other lanthanide oxide powders at the same wavelength. XRD analysis showed that these powders contained a small fraction of lanthanide hydroxide. A well-known fundamental O-H stretching vibration in metal-bound hydroxyl molecules occurs at 2.7–2.86 μm, with the wavelength depending on the metal-oxygen bond strength; therefore, the absorption at 1420 nm is most likely the first

overtone of an O-H stretching vibration in a lanthanide-bound hydroxyl group bound to a lanthanide ion (see also Mara et al. 2019).

In summary, we identify several spectral differences between different Nd-bearing phases: the number and relative depths of the multiplets; the magnitude of the observed small red-shift in the position of the main absorption features; and the absorption features related to the presence of the H_2O molecule or $[OH]^-$, $[CO_3]^{2-}$ and $[PO_4]^{3-}$ functional groups. However, the multiplets are poorly resolved at the current wavelength resolution of modern laboratory spectrometers, let alone UAV- or satellite-based ones. Observed centroid shifts of lanthanide-related absorption features in phosphate versus carbonate are < 5 nm and are probably also outside the scope of most spectrometers. However, in combination, these features produce spectra that can perhaps be distinguished from each other by spectroscopic classification techniques which take the whole spectra into account (e.g., spectral angle method). Especially if wavelength resolutions of field spectrometers and/or hyperspectral cameras improve sufficiently to the point where the narrow multiplets are better resolved (spectral resolution < 1 nm), then the number and depths of the multiplets within an absorption feature can be used to determine the site symmetry of the lanthanide ion, which can help to determine the mineral species hosting the lanthanide ion.

Absorption features of $[PO_4]$ groups are probably too shallow to be used as a diagnostic tool to identify monazite or xenotime. The carbonate absorption near 2355 nm in lanthanide carbonate such as kozoite, however, is probably sufficiently prominent to distinguish REE carbonates from REE phosphates in proximal sensing applications.

Conclusions

1. In this study we showed that single-REE, monazites and xenotimes, multi-element monazite, as well as HREE-doped monazites can be synthesized using a simple precipitation method from a REE phosphate solution followed by heating to 800–900 °C in air. The phase products of this synthesis were confirmed by XRD and structural refinement.
2. We have shown that the visible, near- and shortwave infrared (350–2500 nm) reflectance spectra of synthetic single-REE monazites and xenotimes can be used to identify the REE ions responsible for the absorption features in natural monazites and xenotimes. Trivalent Nd, Pr and Sm are the REE ions which produce the main absorption features in natural monazites. The most diagnostic absorptions in monazite are at wavelengths 580,

745, 800 and 870 nm for Nd^{3+}; at 1080 and 1235 nm for Sm^{3+}; and at 1570 nm for Pr^{3+}. In natural xenotime, trivalent Dy, Er, Ho and Tb ions cause the prevalent absorptions, predominantly in the near- and shortwave infrared regions. Absorptions at 920, 1110, 1260–1350 and at 1700–1800 nm for Dy^{3+}, and at 1500–1600 nm for Er^{3+}, are deemed the most diagnostic.

3. The majority of the REE-related absorption features are caused by excitations of electrons within the 4f subshell of the trivalent lanthanide ions to elevated energy levels resulting from spin-orbit coupling. There are small (< 20 nm) shifts in the wavelengths of these absorptions depending on the nature of the ligands. The energy levels are further split by crystal field effects, which are manifested in the reflectance spectra as closely spaced (c. 5–10 nm in the visible and near-infrared domain, c. 15–20 nm in the > 1000 nm domain) multiplets within the larger absorption features. The number of multiplets and their relative depths are also a function of the coordination symmetry and nature of the ligands. As a result, spectra of different minerals containing the same lanthanide are very similar, but there are some differences that carry information about the ligands and coordination. They may therefore have future applications in proximal or remote sensing for the identification of the minerals hosting the REE, especially as wavelength resolutions of detectors improve.
4. Superimposed on the electronic absorptions are vibrational absorptions in the H_2O molecule or within $[OH]$, $[CO_3]^{2-}$ and $[PO_4]^{3-}$ functional groups, but so far only the carbonate related spectral features seem usable as a diagnostic tool in REE-bearing minerals.
5. The steep drop-off of reflectance values towards lower wavelengths in the visible part of the spectrum associated with a brown colour in many natural monazites is cautiously attributed, pending future research, to the presence of Ce^{4+} and may carry information about redox processes during or after formation of the minerals.
6. Altogether, our results provide a strengthened knowledge base for detection of rare earth elements using reflectance spectroscopy and provides a starting point for the identification of host minerals in mineral resources by means of proximal and remote sensing. Future work could focus on the relation between elemental abundances and the depths of the corresponding absorption features, and thus on obtaining semi-quantitative information about compositions of monazite and xenotimes using hyperspectral data.

Author contributions A.H.D. conceived the project and carried out most of the analytical work. W.H.B. contributed to the project design and processing of the data. F.D. contributed to the XRD analyses and refinement. C.M. carried out most of the reflectance spectroscopy measurements. M.P.P. and H.T.H. advised on the experimental design and analysis of the data. All authors contributed to the writing and reviewing of the manuscript.

Data availability No datasets were generated or analysed during the current study.

Declarations

Ethical approval Not applicable.

Competing interests The authors declare no competing interests.

References

Anenburg M, Burnham AD, Mavrogenes JA (2018) REE redistribution textures in altered Fluorapatite: Symplectites, veins, and phosphate-silicate-carbonate assemblages from the nolans bore P-REE-Th Deposit, Northern Territory, Australia. Can Mineral 56(3):331–354. https://doi.org/10.3749/canmin.1700038

Boesche NK, Rogass C, Lubitz C, Brell M, Herrmann S, Mielke C, Tonn S, Appelt O, Altenberger U, Kaufmann H (2015) Hyperspectral REE (rare earth element) mapping of outcrops—applications for neodymium detection. Remote Sens 7(5):5160–5186. https://doi.org/10.3390/rs70505160

Boesche NK, Rogass C, Mielke C, Herrmann S, Körting F, Papenfuß A, Lubitz C, Brell M, Tonn S, Altenberger U (2016) Hyperspectral rare earth element mapping of three outcrops at the Fen complex, Norway: calcitic, dolomitic, and ankeritic carbonatites. In: Borges de Lima I, Leal Filho W (eds) Rare Earths Industry. Elsevier, pp 235–265. https://doi.org/10.1016/B978-0-12-802328-0.00016-4.

Booysen R, Jackisch R, Lorenz S, Zimmermann R, Kirsch M, Nex PA, Gloaguen R (2020) Detection of REEs with lightweight UAV-based hyperspectral imaging. Sci Rep 10(1):17450. https://doi.org/10.1038/s41598-020-74422-0

Borhan A, Bogdan A, Popa K (2010) On the existence of cerium(IV) orthophosphate $Ce_3(PO_4)_4$. Rev Roum Chim 55(7):389–393

Carnall WT, Crosswhite H, Crosswhite HM (1978) Energy level structure and transition probabilities in the spectra of the trivalent lanthanides in LaF_3 (no. ANL-78-XX-95). Argonne National Lab, Argonne, IL. (United States)

Chen W, Honghui H, Bai T, Jiang S (2017) Geochemistry of monazite within carbonatite related REE deposits. Resources 6(4):51. https://doi.org/10.3390/resources6040051

Clark RN (1999) Spectroscopy of rocks and minerals and principles of spectroscopy. In: Rencz, AN & Ryerson, RA (eds) Spectroscopy and principles of spectroscopy, manual of remote sensing, volume 3, Remote sensing for the Earth Sciences. John Wiley and Sons, ISBN: 978-0-471-29405-4

Clark RN, King TV, Klejwa M, Swayze GA, Vergo N (1990) High spectral resolution reflectance spectroscopy of minerals. J Geophys Research: Solid Earth 95(B8):12653–12680. https://doi.org/10.1029/JB095iB08p12653

Clavier N, Podor R, Dacheux N (2011) Crystal chemistry of the monazite structure. J Eur Ceram Soc 31(6):941–976. https://doi.org/10.1016/j.jeurceramsoc.2010.12.019

Clavier N, Mesbah A, Szenknect S, Dacheux N (2018) Monazite, rhabdophane, xenotime & churchite: vibrational spectroscopy of gadolinium phosphate polymorphs. Spectrochim Acta Part A Mol Biomol Spectrosc 205:85–94. https://doi.org/10.1016/j.saa.2018.07.016

Coint N, Dahlgren S (2019) Rare earth elements (REE) in two long drill-cores from the Fen Carbonatite Complex, Telemark, Norway (preliminary version). NGU report 2019.008. Norwegian Geological Survey. https://www.ngu.no/upload/Publikasjoner/Rapporter/2019/2019_008.pdf (accessed August 2023)

Dieke GH, Crosswhite H, Crosswhite HM (1968) Spectra and energy levels of the rare earth ions in crystals. Wiley Interscience, New York, p 193

Du J, Chen W, Wu G, Song Y, Dong X, Li G, Fang J, Wei W, Sun Y (2020) Evoked methane photocatalytic conversion to C2 oxygenates over ceria with oxygen vacancy. Catalysts 10(2). https://doi.org/10.3390/catal10020196

Eliseeva SV, Bünzli JCG (2010) Lanthanide luminescence for functional materials and bio-sciences. Chem Soc Rev 39(1):189–227. https://doi.org/10.1039/B905604C

European Commission Joint Research Centre (2020) Study on the EU's list of critical raw materials – final report. Publications Office of the European Union, Luxembourg. https://data.europa.eu/doi/10.2873/11619

Freidzon AY, Kurbatov IA, Vovna VI (2018) Ab initio calculation of energy levels of trivalent lanthanide ions. Phys Chem Chem Phys 20(21):14564–14577. https://doi.org/10.1039/C7CP08366A

Goodenough KM, Schilling J, Jonsson E, Kalvig P, Charles N, Tuduri J, Deady EA, Sadeghi M, Schiellerup H, Müller A, Bertrand G (2016) Europe's rare earth element resource potential: an overview of REE metallogenetic provinces and their geodynamic setting. Ore Geol Rev 72:838–856. https://doi.org/10.1016/j.oregeorev.2015.09.019

Griffiths TR, Hubbard HVSA, Davies MJ (1994) Electron transfer reactions in non-stoichiometric ceria and urania. Inorg Chim Acta 225:305–317. https://doi.org/10.1016/0020-1693(94)04062-1

Gysi AP, Harlov D, Costa Filho D, Williams-Jones AE (2016) Experimental determination of the high temperature heat capacity of a natural xenotime-(Y) solid solution and synthetic $DyPO_4$ and $ErPO_4$ endmembers. Thermochimica Acta 627:61–67. https://doi.org/10.1016/j.tca.2016.01.016

House JE (2020) Inorganic chemistry, 3rd edition. Elsevier, 966 pp, https://doi.org/10.1016/C2017-0-01084-4

Hund K, La Porta D, Fabregas TP, Laing T, Drexhage J (2020) The mineral intensity of the clean energy Transition. Climate Smart

Mining Initiative, The World Bank Group, Washington DC, US, https://pubdocs.worldbank.org/en/961711588875536384/Minerals-for-Climate-Action-The-Mineral-Intensity-of-the-Clean-Energy-Transition.pdf

Hunt GR (1977) Spectral signatures of particulate minerals in the visible and near infrared. Geophysics 42(3):501–513. https://doi.org/10.1190/1.1440721

International Energy Agency (2021) The role of critical minerals in clean energy transitions. International Energy Agency, Paris, France. https://www.iea.org/reports/the-role-of-critical-minerals-in-clean-energy-transitions

Jackisch R (2020) Drone-based surveys of mineral deposits. Nat Reviews Earth Environ 1(4):187–187. https://doi.org/10.1038/s43017-020-0042-1

Kokaly RF, Clark RN, Swayze GA, Livo KE, Hoefen TM, Pearson NC, Wise RA, Benzel WM, Lowers HA, Driscoll RL, Klein AJ (2017) USGS spectral library version 7 data: US geological survey data release. United States Geological Survey (USGS): Reston, VA, USA, 61, https://doi.org/10.5066/F7RR1WDJ

Kumar Y, Tripathi S, Nand M, Jangir R, Srihari V, Das A, Singh R, Deshpande U, Jha SN, Arya A (2022) Structural and optical properties of nd doped $LaPO_4$. J Alloys Compd 925:166772. https://doi.org/10.1016/j.jallcom.2022.166772

Liu G, Jacquier B (2006) Spectroscopic properties of rare earths in optical materials, Materials Science Vol. 83, Springer, Berlin-Heidelberg-New York, https://doi.org/10.1007/3-540-28209-2

Lutterotti L, Bortolotti M, Ischia G, Lonardelli I, Wenk HR (2007) Rietveld texture analysis from diffraction images. Z Kristallogr Suppl 26:125–130

Mara D, Artizzu F, Smet PF, Kaczmarek AM, Van Hecke K, Van Deun R (2019) Vibrational quenching in near-infrared emitting lanthanide complexes: a quantitative experimental study and novel insights. Chem Europe 25:15944–15956. https://doi.org/10.1002/chem.201904320

Marien C, Dijkstra AH, Wilkins C (2018) The hydrothermal alteration of carbonatite in the Fen Complex, Norway: mineralogy, geochemistry, and implications for rare-earth element resource formation. Mineral Mag 82(S1):S115–S131. https://doi.org/10.1180/minmag.2017.081.070

Mesbah A, Clavier N, Elkaim E, Gausse C, Ben Kacem I, Szenknect S, Dacheux N (2014) Monoclinic form of the rhabdophane compounds: $REEPO_4 \cdot 0.667H_2O$. Cryst Growth Des 14:5090–5098. https://doi.org/10.1021/cg500707b

Nasdala L, Akhmadaliev S, Burakov BE, Chanmuang C, Skoda R (2020) The absence of metamictisation in natural monazite. Sci Rep 10(1):14676. https://doi.org/10.1038/s41598-020-71451-7

Nazari-Dehkordi T, Spandler C, Oliver NH, Wilson R (2020) Age, geological setting, and paragenesis of heavy rare earth element mineralization of the Tanami region, Western Australia. Miner Deposita 55:107–130. https://doi.org/10.1007/s00126-019-00878-4

Neave DA, Black M, Riley TR, Gibson SA, Ferrier G, Wall F, Broom-Fendley S (2016) On the feasibility of imaging carbonatite-hosted rare earth element deposits using remote sensing. Econ Geol 111(3):641–665. https://doi.org/10.2113/econgeo.111.3.641

Ni Y, Hughes JM, Mariano AN (1995) Crystal chemistry of the monazite and xenotime structures. Am Mineral 80(1–2):21–26. https://doi.org/10.2138/am-1995-1-203

Patrahau I, Singhvi A, Rademaker M, van Manen H, Kleijn R, van Geuns L (2020) Securing critical materials for critical sectors. HCSS Geo-economics, The Hague Centre for Strategic Studies, The Hague, Netherlands, ISBN/EAN: 9789492102805

Percival JB, Abraham AC, Laudadio AB, Sinclair CD (2019) The National Mineral Reference Collection (NMC) Digital Spectral (VIS-NIR-SWIR) Library. Part II: REE-Nb-U-Th-bearing minerals; geological survey of Canada. Open File 8619. https://doi.org/10.4095/315690

Qasim M, Khan SD (2022) Detection and relative quantification of Neodymium in Sillai Patti Carbonatite using decision tree classification of the Hyperspectral Data. Sensors 22(19):7537. https://doi.org/10.3390/s22197537

Reid MF (2016) Theory of rare-earth electronic structure and spectroscopy. In: Bunzli JCG, Pecharsky VK (eds) Handbook on the physics and chemistry of Rare Earths, vol 50. Elsevier, pp 47–64. https://doi.org/10.1016/bs.hpcre.2016.09.001

Rowan LC, Kingston MJ, Crowley JK (1986) Spectral reflectance of carbonatites and related alkalic igneous rocks; selected samples from four north American localities. Econ Geol 81(4):857–871. https://doi.org/10.2113/gsecongeo.81.4.857

Santana IV, Wall F, Botelho NF (2015) Occurrence and behavior of monazite-(Ce) and xenotime-(Y) in detrital and saprolitic environments related to the Serra Dourada granite, Goiás/Tocantins State, Brazil: potential for REE deposits. J Geochem Explor 155:1–13. https://doi.org/10.1016/j.gexplo.2015.03.007

Semwal K, Bhatt SC (2013) Study of Nd^{3+} ion as a dopant in YAG and glass laser. Int J Phys 1(1):15–21. https://doi.org/10.12691/ijp-1-1-3

Shannon RD (1976) Revised effective ionic radii and systematic studies of interatomic distances in halides and chalcogenides. Acta Crystallogr Sect A: Cryst Phys Diffraction Theoretical Gen Crystallogr 32(5):751–767. https://doi.org/10.1107/S0567739476001551

Turner D, Rivard B, Groat L (2014a) Rare earth element ore grade estimation of mineralized drill core from hyperspectral imaging spectroscopy. IEEE Geoscience and Remote Sensing Symposium, July 2014, 4612–4615. IEEE, https://doi.org/10.1109/IGARSS.2014.6947520

Turner DJ, Rivard B, Groat LA (2014b) Visible and short-wave infrared reflectance spectroscopy of REE fluorocarbonates. Am Mineral 99(7):1335–1346. https://doi.org/10.2138/am.2014.4674

Turner DJ, Rivard B, Groat LA (2016) Visible and short-wave infrared reflectance spectroscopy of REE phosphate minerals. Am Mineral 101(10):2264–2278. https://doi.org/10.2138/am-2016-5692

Turner DJ, Rivard B, Groat LA (2018) Visible and short-wave infrared reflectance spectroscopy of selected REE-bearing silicate minerals. Am Mineral 103(6):927–943. https://doi.org/10.2138/am-2018-6195

van Schaik W, Smit SLW, Blasse G (1993) Influence of impurities on the luminescence quantum efficiency of $(La,Ce,Tb)PO_4$. J Electrochem Soc 140:216–222

Van Vleck JH (1937) The puzzle of the rare-earth spectra in solids. J Phys Chem 41(1):67–80

White WB (1967) Diffuse-reflectance Spectra of Rare-Earth Oxides. Appl Spectrosc 21(3):167–171. https://doi.org/10.1366/000370267774385173

Yang C, Yu X, Pleßov PN, Heißler S, Weidler PG, Nefedov A, Studt F, Wang Y, Wöll C (2017) Rendering photoreactivity to ceria: the role of defects. Angew Chem Int Ed 56:14301–14305. doi.org/anie.201707965